Effect of blade modifications on the torque and flow field of radial impellers in stirred tanks

K. Steiros[1], P. J. K. Bruce[1], O. R. H. Buxton[1] and J. C. Vassilicos[1]

[1]*Department of Aeronautics, Imperial College London, SW7 2AZ London, UK*

Abstract

We perform both high and low speed particle image velocimetry and torque measurements to characterize eight radial impeller types in an unbaffled stirred tank. The blade types consist of a set of regular flat blades, used as a baseline, regular blades of increased thickness, perforated blades and fractal blades. We find a qualitative correlation between the blades' torque coefficient and vortex coherence/ turbulent kinetic energy, possibly explaining the torque differences of the tested impellers. Furthermore, we find that the proposed modifications increase the bulk turbulence levels and mass flow rates, while at the same time reducing the shaft torque, showing promise for applications. Finally, we attempt a comparison between fractal and perforated geometries using data from this study and the literature.

1. Introduction

Tanks stirred by radial impellers are extensively used in the process and pharmaceutical industries, in various applications such as gas dispersion and blending of homogeneous liquids. Consequently, extensive research has been conducted during the past decades, aimed at characterizing them and optimizing their performance. The latter has eventually led to the development and characterisation of numerous modifications of the commonly used radial impellers (see for instance [1–12]), in an effort to passively control the flow fields that they generate.

A promising modification type which has recently been introduced is the increase of the blades' perimeter in a fractal manner [1, 3]. The motivation behind this stems from the discovery of some interesting properties of fractal shaped plates, as observed in previous wind tunnel experiments [13, 14]. Specifically, it was shown that fractal shaped plates subjected to a uniform free stream generate wakes with larger values of turbulence intensity and lower shedding compared to square plates of the same frontal area, at the cost of higher drag. The first two properties, if retained in a stirred tank, could prove beneficial for mixing applications, especially when involving shear sensitive substances. Regarding the latter, it would be disadvantageous for the cost of the process, since then fractal shape implementation would mean an increase of power consumption. Nevertheless, experiments [3] and direct numerical simulations [1] in stirred tanks showed that fractal impellers actually exhibit *decreased* torque/ drag over a wide range of *Re*, compared to regular/ rectangular impellers, opposite to what we would expect from the static wind-tunnel experiments. The reason behind this decrease was investigated by Steiros et al. [3], who did not, however, provide a definite answer.

From the above short review we may identify three open questions regarding the usage of fractal blade impellers in stirred tanks: First, the cause of the torque/ drag reduction with respect to the regular/rectangular blades, and the reason this result is reversed in the wind tunnel experiments case. Second, whether fractal blade modification increases the turbulence levels and reduces the shedding in a stirred tank, as suggested from the wind-tunnel experiments. Third, if the power consumption and possible flow field improvements with respect to regular impellers are exclusive to the fractal design, or if they can be reproduced by other modifications as well.

To investigate the above, we perform torque and particle image velocimetry (PIV) measurements in an unbaffled tank; the PIV measurements cover various planes, but an emphasis is given to the blades' discharge region, where the blade wakes and roll vortices are most energetic, and where angle-locked measurements are performed. The tank is stirred by eight different impeller types consisting of a regular impeller used as a baseline, fractal impellers, perforated blade impellers and regular impellers with increased blade thickness. The perforated blades introduce the effect of bleeding to the wake, while an increased thickness has been shown to affect the separation and vortex formation, at least for static bluff bodies in a wind tunnel [15, 16]. Interestingly, when applied in a regular radial impeller, these two

types of modifications have also been shown to decrease the torque in baffled tanks [4–8]. It therefore makes sense to compare them to the fractal impellers.

The structure of the article is as follows: In section 2 we describe the experimental apparatus used in this study; in section 3 we characterize the power consumptions and flow fields of the eight different impeller types; in section 4 we compare the effect of the above modifications implemented in a rotating case (i.e. stirred tank, from this study) and a non-rotating case (i.e. plates subjected to a free stream, taken from literature). We also discuss the similarities of the flow field and drag between fractal and other modifications, for both rotating and non-rotating cases. Finally, in section 5 we draw the conclusions of this study.

2. Experimental configuration

2.1. Stirred tank

Experiments were conducted in an unbaffled, acrylic tank with an inner diameter of $D_T = 45$ cm and height $H = D_T$ (see fig 1). The tank's shape was chosen to be octagonal instead of the conventional cylindrical shape, to avoid optical refraction errors in the PIV measurements. For the same reason a prism filled with water was also attached to the tank's side. An acrylic lid was positioned at the tank top, to minimize free surface displacement. A four-bladed impeller was mounted on the tank mid-height equipped with interchangeable acrylic blades. The impeller's diameter (see fig 1) varied slightly according to the blade type (see table 1), but was always $D \approx D_T/2$. The working fluid was regular tap water.

Eight sets of blades were used (see fig 2 and table 1): A set of regular-rectangular blades (R) with thickness $t = 4$ mm was used as a baseline. Two other sets of identical design were also tested (MT and BT), but with larger thickness, namely $t = 6$ mm and $t = 8$ mm respectively, to test the effect of thickness on the power consumption and flow field. Two fractal blade designs were used (F1 and F2, for details see also [3]) corresponding to fractal iteration numbers of 1 and 2 respectively. In order to establish the effect of the extrusions and cavities in the fractal blades, a perforated blade type (PS) which retained the cavities of the F1 blade, but discarded the extrusions, was also tested. Finally, two types of perforated blades were tested, one with slots and one with circular holes (PG and PC respectively). These two blade types had identical diameter, width and open area ratio S_P/S (perforated over gross blade area) to test the difference between a concentrated perforation on the blade sides and a homogeneous perforation. All blades had the same net frontal area $A = 4228$ mm^2 and, apart from the MT and BT blades, a thickness of $t = 4$ mm. Note that $S = A + S_P$ for PS, PC and PG blades, but $S = A$ for R, MT, BT, F1 and F2 blades. While for the perforated and regular blade types the diameter and width are straightforward to define, this is not the case for the fractal blade types, as they are comprised of many segments. In the following text we used their mean diameter and width, which are the same as for the regular blade types.

The impeller was driven by a stepper motor in micro-stepping mode (25, 000 steps per rotation) to ensure smooth movement, which was controlled by a function generator (33600A, Agilent). Shaft torque was determined with an in-line torquemeter (TM-306, Magtrol) and the rotational speed with an optical encoder (60 ppr). Torque due to friction was monitored by performing tests with the tank emptied of water. The friction torque was then subtracted from the actual measurements.

Blade	R	F1	F2	PS	PC	PG
D (mm)	223	223	223	228.3	230	230
w (mm)	44.8	44.8	44.8	50	50.4	50.4
P (mm)	280	504	935	519	580	601
S_P/S	-	-	-	0.128	0.142	0.142

Table 1: Some dimensions of the impeller types shown in fig 2. D: Diameter. w: Width. P: Blade perimeter. S_P/S: Open area ratio. In all the above impellers the blade thickness is $t = 4$ mm. The impellers MT and BT shown in fig 2 are identical to R, but with blade thickness of $t = 6$ mm and $t = 8$ mm respectively. For the $F1$ and $F2$ impellers their mean diameters and widths are used. All blades had the same net area $A = 4228$ mm^2.
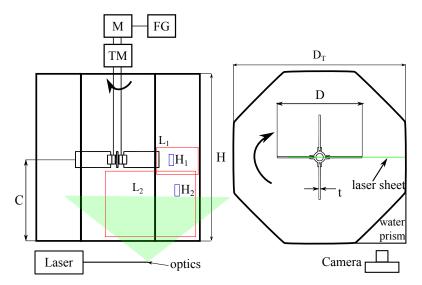
Figure 1: Side and top views of the experimental apparatus. Also shown are the fields of view for the low-speed and high-speed PIV experiments. TM: torquemeter, M: motor, FG: function generator. $D_T = H = 45$ cm. $C = H/2$. $D \approx D_T/2$.
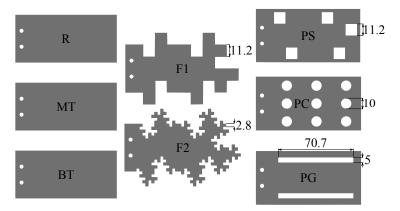

Figure 2: Schematic diagram of the eight different blade types used in the experiments. The indicated dimensions are in mm.

2.2. PIV measurements

Two PIV runs were conducted, one with a low speed system for statistical convergence, where all the blade types were tested, and one with a high speed system to examine the dynamical properties of the flow. In the latter case only the R, F1 and F2 blade types were tested.

Low speed PIV experiments were performed at a shaft speed $N = 3$ Hz corresponding to a Reynolds number $Re \approx 150,000$ ($Re = ND^2/\nu$, ν being the kinematic viscosity of water), in two regions of the tank, namely a small field of view in the impeller discharge region and a large one in the bulk of the flow (L_1 and L_2 respectively in fig 1). Illumination was provided by a Litron Nano L Nd:YAG Laser. A spherical lens and a cylindrical lens were used to obtain a laser sheet of approximately 1 mm thickness, entering the tank from the bottom (see fig 1). The laser sheet was parallel with the z-axis (rotation axis) extending from the centre of rotation to the middle of the side wall. A FlowSense EO 16 MegaPixel camera was used, positioned to the side of the tank, mounted with a 105 mm $f/8$ Nikon lens. The flow was seeded with polyamide 12 powder which consists of particles of 7 μm mean diameter and specific gravity of 1.1.

In the case of the L_1 plane the measurements were angle-locked, in the sense that the camera was conditionally acquiring images at a particular angle between the blade and the laser sheet. This was done by monitoring the function generator's TTL signal via a delay generator (DG645, Stanford Research Systems), which sent a pulse to

the PIV system every 50,000 steps (two full rotations). In that way, images were always synchronised with the same blade. The synchronisation accuracy was checked for the case where the blade was parallel to the laser sheet, and was therefore visible to the camera. No discernible synchronisation loss was evident even after several hundreds of images.

Six planes of 118 mm × 79 mm were monitored, at angles of 0°, 15°, 30°, 45°, 60° and 75° after the impeller passage. The images were acquired in double frame mode. The time between frames was optimized to ensure maximum pixel displacement, without too many losses of particles from the field of view. This time varied slightly with the blade type, but was always in the range 125 to 140 μsec. 400 image pairs were acquired at every plane for each of the eight impeller types, which is enough for the convergence of second order moments [17]. A recursive processing was conducted with an initial window size of 48 × 48 px and a final interrogation region size of 24 × 24 px with a 50% overlap. The number of rejected vectors was always less than 1%. The spatial resolution was 0.58 mm and the vector spacing 0.29 mm, equal in the radial and axial directions. Some of the above experimental features are summarised in table 2.

In the case of the L_2 plane (251 × 169 mm) the images were acquired at approximately 1 Hz. 400 image pairs were acquired for each blade type, with a time between frames ranging from 737 to 775 μsec, depending on the blade type. The vector processing was identical to that used in the L_1 plane, with a resulting spatial resolution of 1.25 mm (see also table 2).

High speed PIV experiments were performed in two planes (see fig 1), one in the impeller stream (H_1), and one in the impeller bulk near the tank side wall (H_2). Only the R, F1 and F2 blade types were tested. Illumination was provided by a Litron LDY300 laser. Similar to the low speed case, the beam passed through a spherical and then a cylindrical lens to create a laser sheet of around 1 mm thickness. A 4 Megapixel Phantom v641 camera was employed, mounted with a 105 mm f/8 Nikon lens. The sensor was cropped (see table 2) to increase the sampling frequency and the acquisition time. Measurements were performed at a shaft frequency of $N = 3$ Hz ($Re \approx 150,000$) in double frame mode. The time between frames was 120 and 400 μsec for the H_1 and H_2 planes respectively, for all tested blade types. The acquisition frequency was set to 1.85 and 1.2 kHz for the two planes respectively, while the acquisition time was 40 and 62.2 s respectively, limited by the camera buffer memory. The final interrogation window size was 32 × 32 px with 50% overlap. The rejected vectors were always less than 1%. The spatial resolution was 1.2 and 1.3 mm respectively, half of the vector spacing.

Plane	Acquisition frequency	Resolution (pixels)	Experimental resolution	Vector count
L_1	Synchronised	4872 × 3248	0.58 mm	406 × 271
L_2	~ 1 Hz	4872 × 3248	1.25 mm	406 × 271
H_1	1850 Hz	80×580	1.2 mm	7×49
H_2	1200 Hz	80×580	1.2 mm	7×49

Table 2: Some experimental parameters of the PIV experiments. The shaft speed was always $N = 3$ Hz corresponding to $Re \approx 150,000$.

3. Results

3.1. Power consumption

In fig 3 we plot the measured torque versus the shaft rotational frequency for each case. We observe a consistent decrease of torque from the baseline case, R, with increasing thickness, when introducing fractal perimeter, or when introducing perforation of the blade. An apparent exception is the PG blade type, which produces almost the same torque as the R.

Conventionally, the torque has been expressed as a power number, i.e. $Np = 2\pi T/\rho N^2 D^5$ [1, 3, 5, 18, 19], where T is the torque, N is the shaft rotational frequency and ρ is the fluid's density. While this way is convenient when all the geometric properties of the impeller scale with the diameter, it may not lead to fair comparisons in cases where the blades have complex shapes, as for instance in the current study where the only common attribute of the blades is the net area. Alternatively, a more representative comparison would occur if the net blade area was also taken into account in the normalisation. In that case, however, two characteristic lengths would be involved in the scaling and
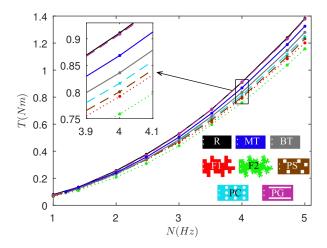
Figure 3: Measured torque over shaft rotational frequency for the eight different blade types. Solid lines: rectangular blades (R, MT and BT). Dashed lines: perforated blades (PS, PC and PG). Dotted lines: fractal blades (F1 and F2).

thus, dimensional analysis would allow infinite possibilities for the torque coefficient. Nevertheless, in Appendix A we argue that, under some assumptions, the torque is in general bounded by the following two scaling laws

$$C_m = \frac{2T}{\rho A \Omega^2 (D/2)^3} \tag{1}$$

$$\tilde{C}_m = \frac{2T}{\rho A^2 \Omega^2 (D/2)} \tag{2}$$

In the above equations $\Omega = 2\pi N$ is the shaft's angular velocity. In fig 4 we plot the two types of torque coefficients of the eight different blade types as a function of Re. For all cases the torque coefficients have a declining trend with Re, a characteristic aspect of unbaffled tanks in the turbulent regime [3, 19]. We observe that for all types of modification (i.e. fractal increase of perimeter, perforation, increase of thickness) both expressions of the torque coefficient are consistently lower compared to the baseline R case. Especially for the fractal and perforated blade types, with the exception of the PG blades, this decrease is more pronounced and relatively similar, even if direct comparison is difficult since for the calculation of the fractal blades' torque coefficient we used their mean diameter in the normalization (see section 2.1) which is not necessarily equal to their effective diameter.

Some secondary conclusions may be drawn by performing a quantitative examination of the torque coefficients. This was done by considering, for each blade, the mean torque coefficient averaged over Re for $Re > 100,000$ (see fig 4), and calculating their percentage differences with respect to the R blades. Note that the percentage differences of the MT, BT, F1 and F2 blades are the same, no matter the choice of torque coefficient type (C_m or $\tilde{C}_m$). We first observe that the torque coefficient drops steadily with increasing thickness, i.e. approximately 4.7% decrease from R to the MT blades and 8.2% from the R to the BT blades. This confirms that this trend, previously observed in Rushton turbines stirring baffled tanks [4–6], can be also found in flat blade turbines stirring unbaffled tanks. However, the decrease in our case is much lower compared to what would be expected in a baffled tank, i.e. 9.2% and 18.5% decrease for our blade types respectively using the correlation formula of [6]. This discrepancy is most probably due to the different impeller type (4-blade flat blade impeller for us and 6-blade Rushton impeller for [6]), and to the change in the flow field caused by the absence of baffles: whereas in baffled tanks the fluid has almost zero tangential velocity, in our case there is a developed solid body rotation which drastically decreases the relative blade velocity.

Comparing the R blades with the three perforated types, we observe a mean decrease in torque coefficient (the values outside and inside the parentheses correspond to differences in C_m and $\tilde{C}_m$ respectively), i.e. 9.6% (3.8%) for the PG blades, 16.7% (12.7%) for the PS blades and 18% (12.6%) for the PC blades. As noted above, the fractal blades also exhibit a drop in torque coefficient with respect to the R type, which increases with iteration number as documented previously by [3] (12.2% and 17% for F1 and F2 respectively). This could be an indication that the torque depends on the iteration number. If this is true, further decrease could be expected for larger iteration numbers.

5

Comparison of the PC and PG blades (which have the same size and open area ratio, see table 1) shows that the same perforation is much more effective in reducing the torque if it is homogeneously distributed compared to it being concentrated at the blade sides. We may therefore conclude that the torque does not scale exclusively with the open area ratio. The torque does not also scale exclusively with the blade perimeter: for instance the torque/ torque coefficient decreases from F1 to F2, while it increases from PC to PG. However, in both cases the perimeter increases (see table 1). Of course, the above does not mean that both the blade perimeter and open area ratio do not affect the torque in any way.
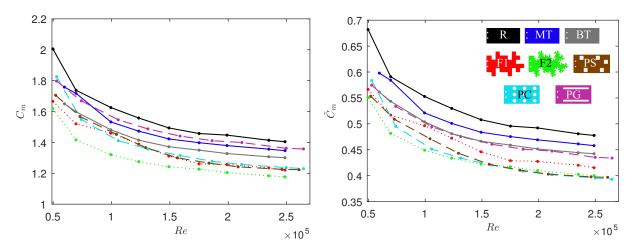

Figure 4: Torque coefficients, defined from eq 1 (left) and eq 2 (right), versus Re, for the different blades. Solid lines: rectangular blades (R, MT and BT). Dashed lines: perforated blades (PS, PC and PG). Dotted lines: fractal blades (F1 and F2).

3.2. Differences in the blades' wake

To investigate the reason behind the torque coefficients' differences, we performed angle-resolved PIV measurements in the L_1 plane (see fig 1) to gain insight regarding the flow separation around the blades. The effect of the conditional averaging process in our planar PIV data is that the computed statistics are the same as if they were calculated in a plane rotating with the impeller speed (neglecting the axial asymmetry of the octagonal tank).

In fig 5 we plot the angle resolved turbulence intensities of the eight different blade types, for 30° after the blade passage, along with vectors corresponding to the conditionally-averaged flow field (not all the vectors are plotted for clarity). The 30° plane was chosen because it contained the most energetic part of the wake. The turbulence intensity is defined as u_t/V_{tip} where $u_t = \sqrt{\langle u_r^2 \rangle + \langle u_z^2 \rangle}$, i.e. the square root of the sum of variances of the conditionally acquired radial and axial velocities, and $V_{tip} = \pi N D$ is a characteristic blade tip velocity for each case. Note that such characteristic velocity choice is arbitrary, something which could affect the comparison of the different blades.

A striking decrease in vortex coherence and turbulence intensities between the baseline (R) and perforated/fractal cases (F1, F2, PS, PC, PG) is immediately noticeable. This decrease is also present in the other measured planes, as shown for instance in fig 6 where the 3D reconstructed angle-resolved turbulence intensities of the R and F2 blade types are plotted. The turbulence intensities and vortex coherence also decrease slightly but consistently with thickness (R, MT and BT blade types), as shown more clearly later in fig 7. From the above we may conclude that there is a qualitative correlation between the torque coefficient (fig 4) and the vortex coherence and intensity. This could suggest that the decrease in the torque coefficient of the modifications may be related to differences in the flow separation mechanism of the blades. By increasing the blade thickness, perforating the blade, or increasing its perimeter in a fractal manner we produce less energetic and coherent vortices; this is known [15] to reduce the wake entrainment, leading to an increase in the base pressure and a decrease in the drag.

Another possibility is that an increase in vortex coherence facilitates the extraction of the angular momentum from the impeller-tank system, resulting in a torque increase via the following feedback mechanism: Assuming that the

more coherent and energetic roll vortices are, the more angular momentum they may carry, then in the case of regular blades, angular momentum is more efficiently transported from its production region (impeller) to its dissipation region (tank walls), contributing to a larger shear there, compared to the other blade types. This would lead to a smaller total angular momentum in the tank, and therefore smaller tangential velocities in the regular case compared to the other blade types. In a sense, regular blades could be thought to introduce a "baffling" effect to the flow, which increases the relative blade velocities, and thus, torque compared to the other blades. The above feedback mechanism, however, does not explain why the torque difference between regular and fractal blades persists in conditions resembling rotation in an infinite medium (i.e. at the start of agitation) [3]. There, solid body rotation is absent in the flow, and may not, supposedly, be abated with the use of regular blades. Furthermore, direct numerical simulations [2] have shown that while regular blades are naturally linked with overall larger dissipation rates in the tank compared to fractal blades (as regular blades input more energy into the flow), the increased dissipation is mainly located in the bulk of the flow, and not in the near wall region, where dissipation profiles are in fact fairly similar for the two blade types. This suggests that, for all blade types, the coherent structures die out before reaching the walls, preventing them from transferring angular momentum there. From the above we may conclude that the feedback mechanism presented above is not the main reason behind the torque decrease when modifying a regular blade.

A secondary point is that the F1, F2 and PS blades produce asymmetric vortices (both in position and intensity), due to the asymmetry of their design (see fig 2). This has repercussions on the pressure distribution of these blades, as shown in [3], where in fact a non-symmetric pressure distribution was found for the F1 blade.

To aid interpretation and to achieve a more quantitative comparison, different statistical quantities have been plotted along a line connecting the two vortex cores (see fig 7). Examples of these lines can be seen in fig 5. In this way the quantities are plotted in the most energetic region of the plane, covering the two vortices and jet region in a similar manner for each blade type. The vortex cores were located by using a simplified version of the λ_2 criterion, introduced by [20], and applying it to the averaged flow fields, but with the actual velocity vectors being replaced by unit vectors, keeping the same orientation as the original. In that way the λ_2 criterion avoided locating points with high shear [21].

In figure 7 the turbulence intensity, u_t/V_{tip}, cross term of the Reynolds stresses, $\langle u_r u_z \rangle$, normalized out of plane vorticity, ω, and radial velocity, U_r, are plotted for all blade types and for angles of 30°, 45°, and 60° after the blade passage. The values correspond to the line connecting the two vortex cores, as described above, with the top vortex corresponding to negative abscissa values. All quantities qualitatively correlate with the torque coefficients (fig 4), especially at the most energetic 30° plane: The R blade type exhibits the largest values, followed by the MT and BT blade types (increased thickness modifications). The PG type follows, with all the other blade types having the smallest and approximately equal values. The F1, F2 and PS blade types have almost identical distributions, showing that large scale characteristics of the flow field of fractals can be generated with perforated blades. Furthermore, their distributions are asymmetrical, reflecting their asymmetric vortex pair (see fig 5). At the 30° plane where the vortices are most clearly formed the turbulence intensity maxima are located on the points of maximum vorticity - near but not exactly on the vortex cores (line edges). There, the fluid's angular velocity assumes very large values, reaching up to 10 times the shaft angular velocity for the R blade type. In the jet region (region around the midpoint of the lines $l = 0$) the turbulence intensities drop significantly due to the acceleration of the fluid. As the blade angle increases (i.e. the wake moves away from the blade) all quantities decrease and tend to collapse, due to diffusion and dissipation acting on the wake.

It is noteworthy to mention that the qualitative correlation of the torque coefficient with the radial jet strength and turbulence intensities/ Reynolds stress term is consistent with the angular momentum balance in the tank: As the impeller torque equals the wall torque (since the system is in a steady state) a blade type which produces larger torque will generate a larger flux of angular momentum towards the walls, especially the side ones. Neglecting the viscous angular momentum transport (a reasonable assumption as the flow is highly turbulent), this flux can be separated into a mean convection part proportional to $U_r U_\theta$ and a turbulent stress part proportional to $\langle u_r u_\theta \rangle$, whose sum must therefore be larger as well. The first term is proportional to the radial jet strength, while the second one can be assumed to be connected with the overall turbulence levels.

Figure 8 shows the trajectory of the vortex cores for the different blade types in the $x - y$ (horizontal) and $\phi - z$ planes, determined by applying the λ_2 criterion in the conditional averaged fields, as previously described. The mean values of the locations of the top and bottom vortices were used for each plane (mean of the absolute values for the case of the $\phi - z$ plane). For the cases of 0° and the 75° planes the core position is not shown as the vortices there
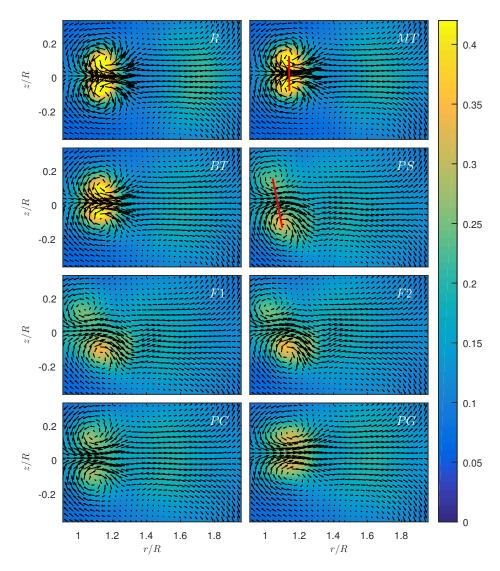
Figure 5: Contours of angle resolved turbulence intensities, u_t/V_{tip}, for the different blade types, 30° after the blade passage. Also plotted are vectors corresponding to the angle resolved mean flow fields. The red lines connecting the vortex cores in the MT and PS cases are examples of the lines along which the quantities of fig 7 are plotted. The normalizing length factor is $R = D_T/4 \approx D/2$.

were not clearly discernible. As the vortices move away from the blades, they are radially displaced towards the wall, influenced by the radial jet. As a result, the blade types with the strongest jet (see fig 7), i.e. the R, MT and BT demonstrate larger radial displacements compared to the other blades. Regarding the axial vortex trajectories ($\phi - z$ plane), the R, MT and BT blade vortex trajectories are the closest to the blade centreline. Comparing these three blade types, we may deduce that increased thickness slightly increases the axial displacement. The fractal and perforated blades vortex core locations are much further away from the blade centreline, due to their increased jet width in these cases, as shown in the next section.

3.3. Impeller pumping capacities and jet widths

To determine the pumping capacities of the different impeller types and their jet widths we perform an effective 360° average by averaging the velocity values of all six planes (0°, 15°, 30°, 45°, 60° and 75°). Examples of the resulting fields can be seen in fig 9 for the R and F2 blade types. The jet width, w_j, was defined as the axial distance
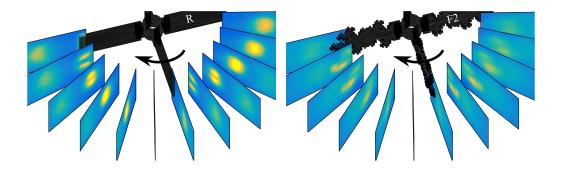
Figure 6: Conditionally averaged turbulence intensities, according to the blade angle, for the R (left) and F2 (right) blade types. From the 12 shown planes only 6 are actually measured, which are presented twice for a clearer view of the wake path. The colourbars are the same as in fig 5.
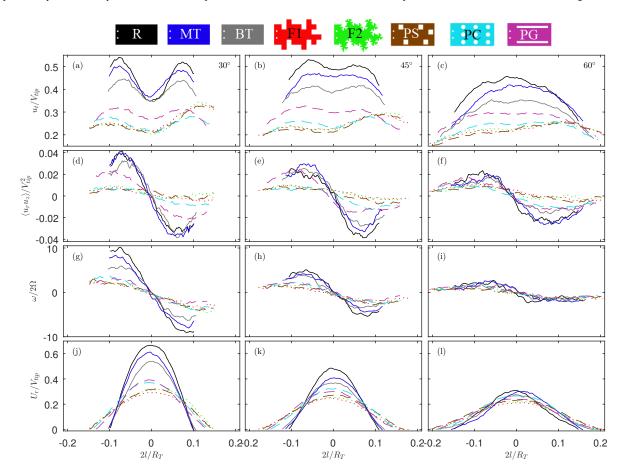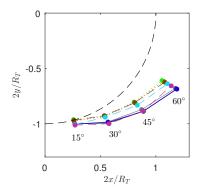

Figure 7: Turbulence intensities, Reynolds-stress cross term, normalized vorticity and radial velocity plotted along the line connecting the two vortex cores for each case, as shown in 5, for the angles of 30°, 45° and 60° after the blade passage (first, second and third columns respectively). The line edges correspond to the vortex cores. Different blade types correspond to different colours, as shown. The normalizing length factor is $R = D_T/4 \approx D/2$. Solid lines: rectangular blades (R, MT and BT). Dashed lines: perforated blades (PS, PC and PG). Dotted lines: fractal blades (F1 and F2).

between the two points of zero radial velocity (solid black lines in fig 9). The mass flow rate is expressed as the non-dimensional mass flow coefficient, defined as
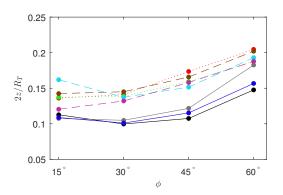
Figure 8: Average vortex core trajectories in the $x-y$ and $\phi-z$ planes for the different blade types. Different blade types correspond to different colours, as shown in fig 7. The normalizing length factor is $R = D_T/4 \approx D/2$. The dashed line in the $x-y$ plane is the $r = R$ locus. Solid lines: rectangular blades (R, MT and BT). Dashed lines: perforated blades (PS, PC and PG). Dotted lines: fractal blades (F1 and F2).

$$C_Q = \frac{2\pi r \int_{z_1}^{z_2} U_r \, dz}{\pi N D A} \tag{3}$$

where the integral limits z_1 and z_2 are set to be the jet limits (black lines in fig 9.) In fig 10 the mass flow coefficients of the different blades are plotted, computed at different radial positions. For all the blade types they are increasing functions of r, due to the entrainment caused by viscosity, similar to a free jet, but also due to additional entrainment caused by the recirculating flow pattern in the tank. Comparing the different blade types we observe that the regular blade types (R, MT and BT) have the smallest mass flow coefficients, slightly increasing with thickness. The PG blades follow, with the fractal and other perforated blade types having the largest pumping capacities. It is interesting that the modified blade types have smaller power consumption compared to the regular blades, but larger mass flow rates, for instance 37% increase for the PS blades compared to the R blades at $r/R = 1.2$. This mass flow rate enhancement in the case of the perforated blades might be one of the reasons behind their higher efficiency in oxygen transfer experiments reported by [7], compared to regular blades.

In fig 10 we also plot the average jet widths of the different blade types, over the radial distance from the centre of rotation. We observe a similar trend with the other flow properties: the regular blade type has the smallest values, followed by the blades of increased thickness and then by the perforated/ fractal blades. The reason for this is presumably the differences in vortex strength and separation between the blade types: as the flow separates from the blades' passage, vortices are generated in the rear side of the blades, which interact with the radial jet (see fig 11). As these vortices grow larger, the effective cross section for the radial jet to pass through is reduced, along with the jet width. Indeed, the jet widths qualitatively correlate with the vortex coherence (for instance the regular blade types demonstrate more coherent vortices and smaller jet width compared to the perforated/ fractal blade types, see figs 5 and 7), suggesting that these two phenomena are linked. Note that the difference in jet width is presumably one of the causes for the difference in the mass flow rate, described in the previous paragraph.

3.4. Bulk turbulence levels

In order to get an idea regarding the performance of the different blade types, planar PIV was conducted in a large field of view in the bulk of the flow (see fig 1) to measure the turbulence intensity levels for the different cases tested. Turbulence intensity might not be the desired end effect of a stirred tank, but it is a crucial factor in numerous processes such as, for instance, scalar mixing or oxygen aeration [8], particularly if it is dominated by incoherent turbulence.

Examples of the measured turbulence intensity fields, u_t/V_{tip}, are shown in fig 12, for the R and PS blade types. In the central white region the camera view was obstructed by the junction area of the prism with the tank. The turbulence intensity fields are similar for the two blade types: Low intensity values are located below the shaft ($2r/R_T \approx 0$), with a column of increased turbulence at ($2r/R_T \approx 0.3$) which is more enhanced in the case of the PS blades. This column
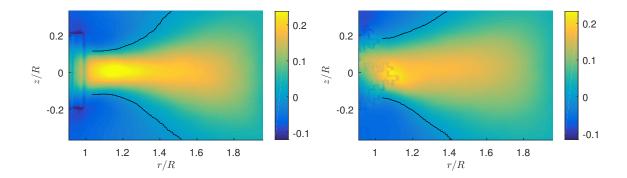
10

Figure 9: Contours of the normalized radial velocity, U_r/V_{tip}, averaged in all 6 measured planes, for the R (left) and F2 (right) blade types. The black solid lines correspond to points of zero radial velocity (jet boundaries). The normalizing length factor is $R = D_T/4 \approx D/2$.
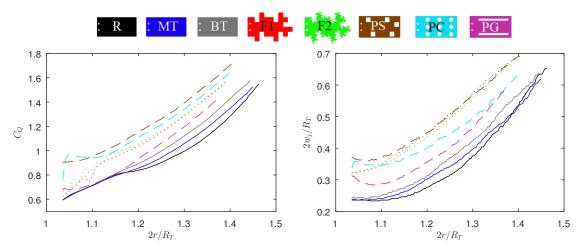

Figure 10: Mass flow rate coefficients (left) and mean jet width (right) over the radial distance from the centre of rotation. The normalizing length factor is $R = D_T/4 \approx D/2$. Solid lines: rectangular blades (R, MT and BT). Dashed lines: perforated blades (PS, PC and PG). Dotted lines: fractal blades (F1 and F2).

is possibly connected with the rear edge of the blades, located at $2r/R_T \approx 0.15$. For larger radii the turbulence levels drop again, until abruptly increasing once more as the tank wall is approached ($2r/R_T = 2$). This increase is larger for the PS blades, probably because of their large jet width (see fig 10), which allows more highly energetic fluid to penetrate the bulk of the flow, instead of reaching the wall region first.

In order to obtain a more quantitative comparison, the turbulence intensity levels of all blade types were averaged in the space covered by the two black boxes in fig 12, with the resulting spatially-averaged turbulence levels plotted in fig 13. The turbulence levels are qualitatively anti-correlated with the torque coefficients (fig 4): The R blade type has the lowest levels, followed by the MT type (3% difference), and then by the BT type (further 3% difference). The perforated and fractal blade types demonstrate a large increase in turbulence intensity, ranging from 19% in the case of the PG blades, to 28.5% in the case of the PS blades. This increase could be one of the reasons, along with the increased mass flow rate (see fig 10), behind the enhanced oxygen mass transfer observed by [7] for the case of perforated blades.

3.5. Turbulence distribution across scales

In the previous sections we measured the turbulence intensities in the discharge and the bulk regions of the tank, to gain an idea regarding the mixing performance of the different impellers. A large turbulence intensity, however, does not guarantee good mixing performance by itself: if turbulence is mainly connected to coherent motion it could actually inhibit mixing, as coherent structures may "trap" fluid particles for an extended period. Knowledge of the
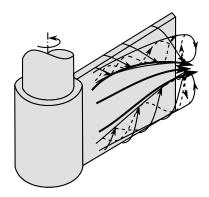
11

Figure 11: Radial jet and roll vortices in the rear side of a rotating flat blade after [22].
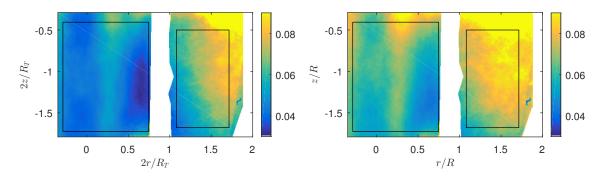

Figure 12: Contours of turbulence intensities, u_t/V_{tip}, for the R and PS blade types (left and right respectively) in the bulk of the flow (L_2 plane in fig 1). The black frames are the limits where spatial averaging of turbulence intensities was performed to create the bar-chart of fig 13. The normalizing length factor is $R = D_T/4 \approx D/2$.

turbulence kinetic energy distribution across scales is therefore necessary, which requires spectral analysis. In this section we present the power spectral densities of the radial velocities of the R, F1 and F2 blade types, as measured in the H_1 and H_2 planes corresponding to the impeller stream and tank bulk planes, as shown in fig 1. The PSDs are plotted at one point per plane only, as the remaining points follow a similar behaviour.

In fig 14 the power spectral densities of the radial velocity in the H_1 plane are plotted, in the position $(r/R, z/R) = (1.3, -0.05)$ with $R = D/2$ and shaft speed $N = 3$ Hz (Re=150,000). Large peaks are visible for all blades at the blade passing frequency (i.e. $f/N = 4$), accompanied by harmonics. These peaks are of similar magnitude in the F1 and F2 cases, while they are much more pronounced and energetic in the R case. Given that these peaks correspond to the periodic passage of the blade wake and roll-vortices, this is a further indication that the R blade type is characterized by a more energetic wake and more coherent vortices; note that the latter may actually inhibit mixing. For higher frequencies the PSDs of the different cases collapse, suggesting a similar small scale behaviour for the different blades. The -5/3 slope fit is quite poor, even if the turbulence levels are very large in this region of the flow, as was also observed by [18].

In fig 14 the power spectral densities of the radial velocity in the H_2 plane are also plotted in the position $(r/R, z/R) = (1.45, -0.78)$ with shaft speed $N = 3$ Hz (Re=150,000). For all three blade types the spectra collapse, and consist of a plateau for frequencies smaller than the impeller rotational frequency, and afterwards an extended -5/3 slope, for almost two decades. No sharp peaks, i.e. coherent motion, are evident. It is noteworthy to mention that the turbulence levels in this region are much smaller compared to the H_1 plane (see fig 12), yet the -5/3 slope is much better defined.

An important point is that the -5/3 slope is predicted when considering spatial scales, while temporal spectra (as the ones presented in fig 14) are expected to exhibit this slope only when a correspondence can be established between time and space via Taylor's frozen hypothesis. That is, when the flow is characterized by a steady advection velocity,
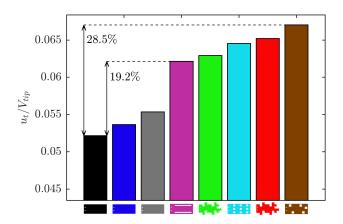
Figure 13: Turbulence intensity levels in the bulk of the flow, spatially averaged inside the black squares of fig 12. The black, blue and gray bars correspond to the R, MT and BT blade types respectively.

which is much larger compared to the velocity fluctuations. In an unbaffled tank, this can be thought to be true for the bulk of the flow, where the the mean tangential velocity due to the developed solid body rotation is much larger than the velocity fluctuations [23]. Near the impeller, turbulence intensities grow significantly, possibly explaining why the -5/3 slope is not that clear there (see fig 14). In any case, the -5/3 slope in temporal spectra has been observed even in flow cases where the Kolmogorov theory conditions for its existence are very far from being met [24–26] which means that its underlying cause remains fundamentally unexplained not only in our flow but also in general.

4. Discussion

4.1. Drag/torque of rotating and non-rotating modified plates

As discussed in the introduction, modifying a bluff body may create opposite results in its drag, depending on whether the body is performing a rotating or a translating motion. Specifically, certain types of fractal modification of a square plate's perimeter have been shown to increase the drag when the plate is subjected to a uniform flow [13]. However, when modifying rectangular solid blades with similar fractal modifications, the torque and drag show a decreasing trend [1, 3]. The latter was shown for both steady state operation and for the period immediately after the initiation of stirring a quiescent fluid, which resembles the rotation of the impeller in an infinite medium [3, 27]. In this section we check in the existing literature whether a similar behaviour between rotating and translating motions can be observed for the other modifications investigated in this study (i.e. increased thickness, perforation).

The effects of thickness on an infinite plate subjected to a uniform stream have been studied in detail by Bearman and Trueman [15] and Norberg [16] among others. They found that, starting from an infinitely thin plate and increasing the thickness to width ratio (t/w), the drag increases until $t/w \approx 0.6$ whereby the drag starts decreasing. As was explained by [15], initially, a thickness increase moves the plates' rear side closer to the shed vortices, increasing the drag. However, after a certain thickness ratio (i.e. $t/w \approx 0.6$) the rear corners of the plate (or better now prism) start interfering with the separated shear layer, causing a drop in the drag. The impeller blade thickness to width ratio used in the current study ranges from 0.09 to 0.18, while for Chapple et al. [4] and Bujalski et al. [5] who used baffled tanks, from 0.05 to 0.17, in all studies being smaller than the 0.6 "limit" mentioned above. Nevertheless, for all cases the torque has a declining trend with increasing blade thickness ratio, *opposite* to what we would expect following the rationale presented above.

Next, we compare rotating and non-rotating perforated plates. Regarding the rotating case, we saw that the three types of perforation used in this study caused a decrease in the torque coefficient, compared to the regular blade' torque coefficient (see section 3.1), something also reported previously for Rushton turbines stirring baffled tanks [7, 8]. Regarding the non-rotating case, perforated plates subjected to a uniform free stream have been widely investigated by [28–31] among others. de Bray [31] in particular used a drag balance to measure the drag of perforated square thin
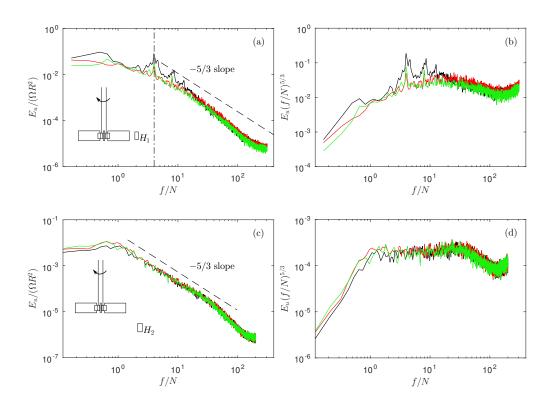
13

Figure 14: Radial velocity PSD (left) and compensated PSD with $(f/N)^{5/3}$ (right) of the R, F1 and F2 blade types (black, red and green colours respectively) in the H_1 (top) and H_2 (bottom) planes. The shaft speed was 3 Hz corresponding to $Re \approx 150,000$. The dashed-dotted line denotes the blade passing frequency.

plates, with different open area ratios (i.e perforated area over gross area, S_P/S) but always the same gross area, S. The plates had either homogeneous or concentrated perforations. Comparing the drag per gross area of the different plates, de Bray [31] showed that the drag decreases with perforation, i.e. as the net area of the plates decreased.

We now want to determine the resistance capability of a given solid area, taking different shapes (i.e. fractal, solid rectangle, perforated). For this reason we use the drag coefficient expressed as the drag per actual (net) area of the solid. In fig 15 we plot these drag coefficients for the depicted perforated plates versus their open area ratio, using data taken from de Bray [31]. A solid and a fractal plate [14] are also included. We observe that the drag coefficient of a solid plate generally increases with perforation, opposite to the torque coefficient of the rotating case, but a slight decrease is also possible when the perforation is concentrated in the outside of the square and S_P/S takes values comparable to those in table 1, much similar to the rotating case. In his original work, de Bray also measured the drag of additional perforated plates (e.g central perforations of varying open area ratio) which we do not show here for clarity; we note however that the drag normalized with the net area assumes larger values than the one of the solid plate, while it follows a generally increasing trend with S_P/S. We may therefore conclude that there can be some cases of perforation where the torque coefficient of a rotating blade may exhibit an opposite trend trend to that of the drag coefficient of a non-rotating plate, but also some cases of perforation where they may behave similarly. It is important to mention that since the net area of the plates of de Bray [31] changes with perforation, $Re = \sqrt{A}U_\infty/\nu$ changes as well (see fig 15). Nevertheless, this does not seriously affect our conclusions, as the drag coefficient is Re independent in the fully turbulent regime, at least when considering a solid square plate [13].

4.2. Comparison of fractal and perforated plates

In section 3 we saw that the fractal and some perforated blade types tested in this study, have various similarities, especially as opposed to the R blades. Specifically, these blade types exhibit similar torque coefficient values, which are significantly reduced compared to the R blades (see section 3.1). Furthermore, they exhibit similar vortex
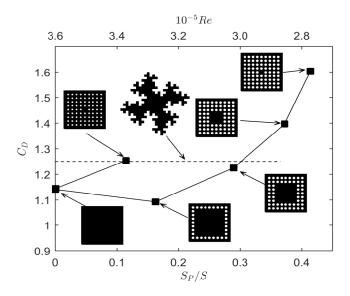
Figure 15: Drag coefficients of plates as a function of their open area ratio and their *Re*, taken from de Bray [31], using the net plate area when calculating the C_D and *Re*. Also plotted with the dashed line is the maximum documented drag coefficient of fractal plates, corresponding to the $D_f = 1.5(2)$ fractal plate [13].

coherence, turbulence intensity values, vortex path trajectories and mass flow rates (see section 3.2), all of them much different from the R case. Finally, the turbulence intensities of the these types in the bulk region have similar values, and are much larger than the ones corresponding to the R blades. Given the above, it would be interesting to investigate if similarities exist between the fractal and perforated geometries in the non-rotating case as well (i.e. plates subjected to a free stream).

As shown by Nedić et al. [13], certain types of fractal modification of a plate's perimeter can cause a non-negligible increase in the drag coefficient. This was deemed important as, until then, it was generally believed that the drag coefficient is insensitive to the plate's rim. An example of this increase in drag coefficient can be seen in fig 15, where the maximum documented drag coefficient of fractal plates is plotted, corresponding to the $D_f = 1.5(2)$ fractal plate in reference [13]. As can be seen in fig 15, perforation can also increase the drag coefficient to similar levels and even higher; for instance a similar drag coefficient of the depicted fractal plate can be achieved by perforating the two outer rows of a solid square. It must be noted however that, in the case of fractal plates, the extent of the drag change was shown to be dependent on the iteration number and fractal dimension of the plate. In fact, for the $D_f = 1.3$ plates a small but monotonically increasing trend of the drag coefficient with iteration number was observed, while for the $D_f = 1.5$ plates the increase was larger, but the trend was first increasing, and then decreasing to almost the same levels as the original square plate. Such trends do not agree easily with the trend of perforated plates. In fact, the increasing fractal iteration and increasing perforation trends cannot even be compared, primarily because we would need an unambiguous correspondence between fractal iteration number and free area ratio. Therefore, it is not possible to ascertain , apart from some similarities, the drag coefficients of the two plate types are determined by the same physical mechanisms.

Another significant effect of the fractal modification of a static plate, is the decrease of the shedding intensity, this being more accentuated as the iteration number of the plate increases [13]. We now perform a comparison between the measured spectra of two studies, i.e from de Bray [31] involving perforated plates and from Nedić et al. [13] involving fractal plates. In both studies the flow was fully turbulent and the spectra were measured via a hot-wire anemometer at a radial position of $r \approx 0.8\sqrt{A}$ from the square plates' centre point, where the maximum fluctuations occurred. However, the measurements for Nedić et al. [13] were located at $5\sqrt{A}$ downstream distance from the plates (all plates had the same net area, *A*, in this study), whereas for de Bray [31] this varied depending on the plate (as his perforated plates had the same gross, but different net areas). Specifically, for the square plate this distance was $3.6\sqrt{A}$ downstream of the plate, and for the perforated plate with two rows open $4.3\sqrt{A}$ downstream. We nevertheless carry out a qualitative comparison. In fig 16 we plot the pre-multiplied spectra, $f \cdot E$, from the two studies as a function of

15

the Strouhal number, $St = f \sqrt{A}/U_\infty$. The curves involve a fractal and a solid square plate, and a perforated and a solid square plate as shown. The pre-multiplied spectra of each study were normalized with the corresponding maximum value of the solid square plate $f_s \cdot E_s$, to enable comparison of the two experiments. Both fractal and perforated plates reduce the shedding, compared to the square plate, and their spectra would appear to almost collapse. It is important to mention, however, that there is no reason to expect this collapse to be any more than coincidental, as the measurements were not acquired in the same downstream distance for the two studies, as noted above, while in the case of de Bray, the plates did not have the same characteristic length and Reynolds number, i.e. 15% difference in $\sqrt{A}$ and Re. From the above, we may conclude that both fractal and perforated plates excite flow mechanisms which mitigate the shedding. However, the currently available data are not sufficient to check how similar these mechanisms actually are.
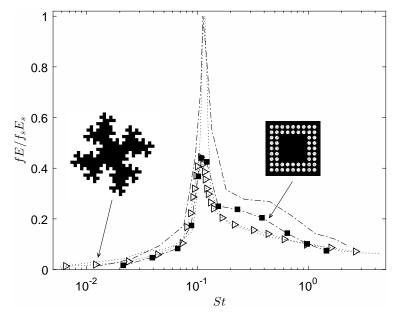

Figure 16: Pre-multiplied spectra of various plates as a function of the Strouhal number based on the net plate area. Dashed-dotted lines: data taken from de Bray [31], including a solid square (no symbols) and a perforated plate (squares). Dotted lines: data taken from Nedić et al. [13] including a solid square (no symbols) and the fractal plate $D_f = 1.5(2)$ (triangles). The spectra are normalized with the peak spectral value of the corresponding solid square plates of each study, to enable comparison of the two experiments.

5. Summary and conclusions

The aim of this article is to answer the following three open questions regarding fractal bladed impellers in stirred tanks, as presented in the introduction: First, the reason fractal impellers generate smaller drag/torque compared to regular-rectangular bladed impellers, and why this is opposite to the wind tunnel experiments, where fractal plates generated more drag compared to square plates of the same area. Second, whether the flow field of fractal impellers is characterized by larger turbulence intensities and lower shedding compared to the flow field of regular impellers, both important for applications, as suggested from wind tunnel experiments. Third, if flow field properties of the fractal impellers can be reproduced by other geometries as well. The latter is important, because it could give us important information regarding the flow mechanisms introduced by the fractal geometries.

To answer the above, eight versions of a flat blade turbine equipped with either regular-rectangular blades (baseline case) and seven modifications of the baseline case were experimentally compared in an unbaffled stirred tank using low and high speed planar PIV and torque measurements. The blade modifications included two rectangular sets of blades identical to the baseline but with larger thickness, three types of perforated blades, and two types of fractal blades. All blade types had the same net frontal area.

It was found that the torque of all modifications decreased compared to the baseline case: the fractal and some perforated blade types in particular demonstrated the largest and relatively similar decrease, while the torque was a decreasing function of the blade thickness. A qualitative correlation between the torque coefficient and vortex coherence and turbulent kinetic energy was found, suggesting that the drop in torque is due to the weakening of large scale vortices. The latter is known [15] to diminish the wake entrainment and increase the base pressure, ultimately leading to a decrease in drag.

The overall bulk turbulence levels of fractal and perforated blades were found to be larger compared to the baseline case. Moreover, the mass flow rates of these modifications were significantly enhanced compared to the baseline case. This led to the interesting conclusion that the proposed modifications decrease the power demand and increase the generated turbulence and mass flow rates, something which could prove useful for practical applications.

The torque and flow fields generated by the particular fractal blades tested here were found to have various similarities to the ones generated by some perforated blades. To investigate whether there is some generality in this, we performed a literature review to find out whether the fractal and perforated designs have similarities in the non-rotating case as well, i.e. for plates subjected to a free stream. It was found that two flow properties (i.e. drag coefficient and shedding intensity) of both plate types demonstrated qualitative similarities. However, the same flow properties exhibited unique trends for each case, a fact which did not allow the assertion that the two shapes excite the same physical mechanisms.

The reason fractal modification of the perimeter reduces the drag in the rotating case (i.e. stirred tank), while it increases the drag/torque in the non-rotating case (i.e. plates subjected to a free stream) could not be answered and remains open. Interestingly, by performing a literature review it was found that an opposite trend in the torque/drag coefficients between the rotating and non-rotating cases is possible to appear for other modifications, i.e. increased thickness and introduction of perforation.

Appendix A. Derivation of the torque coefficients

We first assume that the power input in the tank scales with the energy dissipated in the volume of revolution of the impeller blades, i.e.

$$T\Omega \sim A2\pi R_m \rho \bar{\epsilon} \tag{A.1}$$

where $A2\pi R_m$ is the volume of revolution of a given blade (R_m is the blade's centroid radius) and $\bar{\epsilon}$ is the mean dissipation rate in that volume. We assume that the latter scales as

$$\bar{\epsilon} \sim l^2 \Omega^3 \tag{A.2}$$

where l is a characteristic length scale. This may be assumed to scale with the blade radius and square root of net area, i.e. $l \sim R^a \sqrt{A}^b$ with $a + b = 1$. If we assume that approximately $R_m \sim R$, we have the two extreme cases for the torque coefficient, i.e. $a = 1$, $b = 0$ and $a = 0$, $b = 1$ which lead to eqs 1 and 2 respectively. In the specific case of regular impellers we have approximately $A \sim Rw$, where w is the blade width. Additionally, it is often assumed that $T \sim w$, but experimental correlations show that $T \sim w^k$, where $1 \leq k \leq 1.25$ [32]. From eqs A.1, A.2 and $l \sim R^a \sqrt{A}^b$, this could suggest $0 \leq b \leq 0.25$ for regular blades, which is closer to equality 1 than to 2. For fractal and perforated blades no such correlations are available.

Acknowledgments

References

[1] S. Başbuğ, G. Papadakis, and J. C. Vassilicos. DNS investigation of the dynamical behaviour of trailing vortices in unbaffled stirred vessels at transitional Reynolds numbers. *Phys. Fluids.*, 29:064101, 2017.

[2] S. Başbuğ, G. Papadakis, and J. C. Vassilicos. Reduced energy consumption in stirred vessels by means of fractal impellers. *arXiv*, 1707.01730, 2017.

[3] K. Steiros, P. J. K. Bruce, O. R. H. Buxton, and J. C. Vassilicos. Power consumption and form drag of regular and fractal- shaped turbines in a stirred tank. *AIChE J.*, 63(2):843–854, 2017.

[4] D. Chapple, S. M. Kresta, A. Wall, and A. Afacan. The effect of impeller and tank geometry on power number for a pitched blade turbine. *Chem. Eng. Res. Des.*, 80(4):364–372, 2002.

[5] W. Bujalski, A. W. Nienow, S. Chatwin, and M. Cooke. The dependency on scale of power numbers of Rushton disc turbines. *Chem. Eng. Sci.*, 42(2):317–326, 1987.

[6] K. Rutherford, S. M. S. Mahmoudi, K. C. Lee, and M. Yianneskis. The influence of Rushton impeller blade and disk thickness on the mixing characteristics of stirred vessels. *Trans. IChemE, Part A, Chem. Eng. Res. Des.*, 74(A3):369–378, 1996.

[7] R. V. Roman, Z. R. Tudose, M. Gavrilescu, M. Cojocaru, and S. Luca. Performance of industrial scale bioreactors with modified Rushton turbine agitators. *Acta Biotechnol.*, 16(1):43–56, 1996.

[8] J. T. Vasconcelos, S. C. P. Orvalho, A. M. A. F. Rodrigues, and S. S. Alves. Effect of blade shape on the performance of six-bladed disk turbine impellers. *Ind. Eng. Chem. Res.*, 39(1):203–213, 2000.

[9] F. Ravelet, A. Chiffaudel, F. Daviaud, and J. Léorat. Toward an experimental von Kármán dynamo: Numerical studies for an optimized design. *Phys. Fluids*, 17:117104, 2005.

[10] L. Marié and F. Daviaud. Experimental measurement of the scale-by-scale momentum transport budget in a turbulent shear flow. *Phys. Fluids*, 16(2):457–461, 2004.

[11] F. Ravelet. Bifurcations globales hydrodynamiques et magnétohydrodynamiques dans un écoulement de von Kármán turbulent. *Ph.D. thesis*, École Polytechnique, 2005.

[12] L. Marié. Transport de moment cinétique et de champ magnétique par un écoulement tourbillonnaire turbulent: Influence de la rotation. *Ph.D. thesis*, Université de Paris 7, 2003.

[13] J. Nedić, B. Ganapathisubramani, and J .C. Vassilicos. Drag and near wake characteristics of flat plates normal to the flow with fractal edge geometries. *Fluid. Dyn. Res.*, 45(6):061406, 2013.

[14] J. Nedić, O. Supponen, B. Ganapathisubramani, and J. C. Vassilicos. Geometrical influence on vortex shedding in turbulent axisymmetric wakes. *Phys. Fluids*, 27(3):1–17, 2015.

[15] P. W. Bearman and D. M. Trueman. An investigation of the flow around rectangular cylinders. *Aeronaut. Quart.*, 23:229, 1972.

[16] C. Norberg. Flow around rectangular cylinders: Pressure forces and wake frequencies. *J. Wind Eng. Ind. Aerodyn.*, 49:187–196, dec 1993.

[17] Z. Li, Y. Bao, and Z. Gao. PIV experiments and large eddy simulations of single-loop flow fields in Rushton turbine stirred tanks. *Chem. Eng. Sci.*, 66(6):1219–1231, 2011.

[18] H. Wu and G. K. Patterson. Laser-Doppler measurements of turbulent-flow parameters in a stirred mixer. *Chem. Eng. Sci.*, 44(10):2207–2221, 1989.

[19] D. S. Laity and R. E. Treybal. Dynamics of liquid agitation in the absence of an air-liquid interface. *AIChE J.*, 3(2):176–180, 1957.

[20] R. Escudié and A. Liné. A simplified procedure to identify trailing vortices generated by a Rushton turbine. *AIChE J.*, 53(2):523–526, 2007.

[21] P. G. Kapiris and D. S. Mathioulakis. Experimental study of vortical structures in a periodically perturbed flow over a backward-facing step. *Int. J. Heat Fluid Fl.*, 47:101–112, 2014.

[22] S. Winardi and Y. Nagase. Characteristics of trailing vortex (discharged wake vortex) produced by a flat blade turbine. *Chem. Eng. Commun.*, 129(1):277–289, 1994.

[23] J. N. Haque, T. Mahmud, K. J. Roberts, J. K. Liang, G. White. D. Wilkinson and D. Rhodes. Free–surface turbulent flow induced by a Rushton turbine in an unbaffled dishbottom stirred tank reactor: LDV measurements and CFD simulations. *Can. J. Chem. Eng.*, 89:745–753, 2011.

[24] F. Alves Portela, G. Papadakis, and J. C. Vassilicos. The turbulence cascade in the near wake of a square prism. *J. Fluid Mech.*, 825:315–352, 2017.

[25] R. Gomes Fernandes, B. Ganapathisubramani, and J. C. Vassilicos. The energy cascade in near-field non-homogeneous non-isotropic turbulence. *J. Fluid Mech.*, 771:676–705, 2015.

[26] S. Laizet, J. Nedić, and J. C. Vassilicos. The spatial origin of -5/3 spectra in grid-generated turbulence. *Phys. Fluids*, 27(6):065115, 2015.

[27] D. Maynes and M. Butcher. Steady-state and decay dynamics for impellers of varying aspect ratio in unbaffled tanks. *AIChE J.*, 48(1):38–49, 2002.

[28] I. P. Castro. Wake characteristics of two-dimensional perforated plates normal to an air-stream. *J. Fluid Mech.*, 46(3):599–609, 1970.

[29] G. I. Taylor. Air resistance of a flat plate of very porous material. *Aero. Res. Counc. R & M no 2236*, 1944.

[30] J. M. R. Graham. Turbulent flow past a porous plate. *J. Fluid Mech.*, 73(3):565–591, 1976.

[31] B. G. de Bray. Low speed wind tunnel tests on perforated square flat plates normal to the airstream : drag and velocity fluctuation measurements. *Aero. Res. Counc. CP*, 323, 1957.

[32] L. R. Bates, P. L. Fondy, and R. R. Corpstein. An examination of some geometric parameters of impeller power. *Ind. Eng. Chem. Process Des. Dev.*, 2:310–314, 1963.